Publications of the Astronomical Society of the Pacific, 134:074501 (11pp), 2022 July https://doi.org/10.1088/1538-3873/ac6699

Short-exposure Image Reconstruction with The Power Spectrum Extended (PSE) Method

É. Cottalorda[1,2], É. Aristidi[1], M. Carbillet[1], M. Guinard[2], M. Pyanet[2], and S. Vourc'h[2]
[1] Université Côte d'Azur, Observatoire de la Côte d'Azur, CNRS, Laboratoire Lagrange, Parc Valrose, F-06100 Nice, France
[2] ArianeGroup, 51/61 route de Verneuil, BP 71040, F-78131 Les Mureaux Cedex, France
Received 2021 July 8; accepted 2022 April 11; published 2022 July 18

Abstract

We analyze, in the framework of high angular resolution imaging, a novel image reconstruction method denoted as PSE (which stands for power spectrum extended). It works in the Fourier space, combining the information from both the average power spectrum of the images and a phase estimation from an ad-hoc shift-and-add process. PSE allows to perform image reconstruction up to the diffraction limit of the telescope from a series of short-exposure frames, with a refined lucky-imaging selection process. The method is well adapted to partially corrected adaptive-optics images, in particular in case of low Strehl corrections, and/or small diameter telescopes. In this paper we analyze the PSE technique by means of Monte-Carlo simulations and compare it with the ISFAS lucky-imaging method. Comparative performances were investigated using three metrics: Strehl ratio for reconstructed point-like sources, intensity ratio for binary stars, and least-square distance between images for a simulated artificial satellite. We found that PSE provides an improvement of a factor ∼2 over ISFAS on the Strehl ratio in the case of faint point sources. It seems also to give better images reconstruction on some kinds of extended objects (planets or binary stars with small magnitude difference). PSE has also the advantage to be very fast and well adapted to real-time image reconstruction.

Unified Astronomy Thesaurus concepts: Astronomy software (1855); Artificial satellites (68); Astronomical methods (1043)

1. Introduction

Atmospheric turbulence limits observations of astronomical objects and artificial satellites from ground-based telescopes as soon as the Fried parameter r_0, defining the length of the spatial coherence areas on the incoming perturbed wave front Fried (1966), becomes smaller or of the order of the telescope diameter D. In a long-exposure image formed at wavelength λ, the diffraction-limited resolution λ/D ($0\farcs1$ in the visible with a 1 m aperture) is so overcome by the turbulence-induced resolution λ/r_0 ($1''$ with a typical 10 cm r_0).

As demonstrated by Labeyrie in its seminal paper Labeyrie (1970), this turbulence-induced (variable in time) blurring effect can be frozen when taking short exposures. The results are (non averaged) speckle patterns, but still contain the high angular resolution (HAR) information which can be uncovered in the Fourier space. The speckle interferometry (SI) method Labeyrie (1970) hence computes the power spectrum of both the images of the observed object and a reference star in order to deduce a quantity, the visibility, which belongs to the observed object characteristics only. But, the power spectrum being a modulus squared, any asymmetric information is lost. The necessity to retrieve, in addition to the modulus of the Fourier transform (FT), its phase, is hence at the heart of the HAR techniques. Some advanced speckle processing algorithms exist, such as the Knox-Thompson method Knox & Thompson (1974) or the bispectrum technique Weigelt (1991), but they turn out to be quite heavy in terms of computation time.

The retrieval of HAR information can also be helped by lucky imaging (LI), the idea behind LI being that there is an interestingly non-null probability to obtain a short-exposure image with a resolution close to the diffraction limit Fried (1978). With the advent of very low read-out noise camera in the visible Basden et al. (2004), Baldwin et al. (2001) first proposed an LI algorithm composed of an image selection stage followed by a simple method, shift-and-add (SaA) Baba et al. (1985). The combination of LI and adaptive optics (AO) correction (see, e.g., mackay et al. 2012), which primary goal is to enhance image quality, represents hence a quite natural idea since, as pointed out by Femenía et al. (2011), such an association permits to use a large fraction of data in the image selection and/or equivalently to keep better quality images.

In the present article, we analyze a novel LI method, the power spectrum extended (PSE) technique, combining SI for the reconstruction of the modulus of the Fourier transform of the image of the observed object, and an estimation of the corresponding phase from an ad-hoc SaA method, together with a proposed selection of the best short exposures.

Preliminary results using PSE were already presented elsewhere Cottalorda et al. (2019), Aristidi et al. (2020), including a presentation on the results obtained on simulated post-AO data Cottalorda et al. (2020). Here, we rather focus on a detailed description of the method itself and its analysis, using numerical simulations.

The paper is organized as follows. The global scheme and different steps (selection, alignment, reconstruction in the Fourier space) of PSE are described in Section 2. A comparison of the performance obtained with respect to one of the most efficient LI algorithm, "Image Synthesis based on the Fourier Amplitude Selection" (ISFAS) Garrel et al. (2012), is presented in Section 3, on simulated point-spread functions (PSF) first, and then on simulated images of binary stars and an artificial satellite. Eventually, a summary and a conclusion are given in Section 4.

2. The Method

PSE is a LI method which works on time series of short-exposure images of an object which is then tentatively reconstructed up to the diffraction limit of the telescope. It combines a LI process and a SI technique, the main idea being to compute a SaA image from a selection of short-exposure frames, and to replace the modulus of the FT of this image by the square root of the average power spectrum of individual frames Labeyrie (1970), which contains more information than a simple SaA. Hence, and this is one of the originality of the PSE method, the reconstruction of the modulus and the phase of the FT of the image are performed separately. In addition, and in order to improve the global reconstruction process, we propose the amelioration of two important steps of the LI process: the frame selection and the centroid calculation.

The PSE algorithm can be divided into five steps, detailed here below.

1. Selection of the best images, using a criterion based on the evaluation of an instantaneous Fried parameter (Section 2.3).
2. Alignment of short-exposures in the time series. We propose an alignment based on the phase difference of the FT of successive images (Section 2.4).
3. On selected images: computation of the average power spectrum. The square root of the power spectrum is then taken as an estimate of the modulus of the FT of the object.
4. On selected images: add all frames to obtain a SaA image, and take the phase of its FT.
5. Using the modulus and phase above, invert the FT to obtain the PSE reconstructed image.

The idea of point (iii) is that the square root of the power spectrum contains more information than the modulus of the FT of the long-exposure image, thus leading to a reconstructed image with more details. However, it should be noted that there is no compensation of the speckle transfer function (STF) in our present algorithm, as it is done in Labeyrie's original speckle interferometry technique. Indeed, PSE belongs to the LI family where STF compensation is generally not made (see for example Garrel et al. 2012). STF compensation could however be considered with PSE in the future, using either a modeling such as in Tokovinin (2010), or by subtracting the cross-spectrum of images separated by a temporal lag greater than the coherence time, as proposed by Worden et al. (1977) and used routinely for speckle observations with the PISCO speckle camera Scardia et al. (2019).

In the following, the algorithm is tested on images distorted by turbulence, both from numerical simulations and real observations (Section 2.1). The simulations performed are described in Section 2.2, while a detailed description of the steps of the method are presented in the two subsequent subsections.

2.1. Application on Observations Data

We present in this section an application of the PSE method on real speckle data. Figure 1 shows two examples of image reconstruction, on a binary star and on the planet Saturn. The binary star β Del (Figure 1, left) was observed in the R-band with the 2 m Bernard-Lyot telescope at the Pic du Midi, France (see Aristidi et al. 1997 for details on these observations). The image cube contains 320 short-exposure frames, with a ratio $D/r_0 \simeq 15$. The reconstruction was made from a selection of the 20% best frames, i.e., 64 images. Despite this small number of instantaneous images, and the high D/r_0 ratio, we can see that the binary star image appears well restored by PSE.

For the image of Saturn (Figure 1, right), observations were performed in the visible ($\lambda = 700$ nm) with a 35 cm telescope. The image cube contains 1000 short-exposure frames, with an exposure time of 50 ms, from which we selected the 20% best images. The angular diameter of the planet together with its rings is about 45″, which is much larger than the isoplanatic angle. The image of the planet shows details close to the diffraction limit of the telescope.

2.2. Simulations

The simulated data used in this paper were generated by means of the `Software Package CAOS` Carbillet et al. (2005, 2016), part of the `CAOS Problem-Solving Environment`, and considering one of the two 1.04 m telescopes of the "Centre Pédagogique Planète Univers" (C2PU) Bendjoya et al. (2012), at the plateau de Calern, Observatoire de la Côte d'Azur, France. These data consist in cubes of 1000 short-exposure images of a point-source in the visible-red spectral domain, with 4 pixels per resolution element λ/D, and for various turbulence conditions. These conditions are characterized by Fried parameters r_0 values of

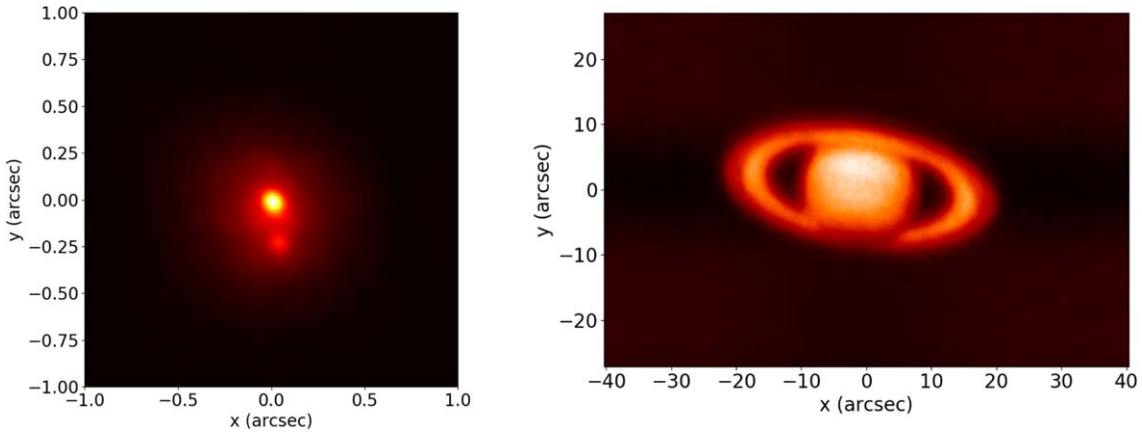

Figure 1. Left: PSE image of the double star β Del, from a set of 324 speckle images in the visible (654 nm), at the focus of a 2 m telescope. The selection rate for this reconstruction is 20%. Right: PSE image of Saturn from a set of 1000 images at a wavelength of 700 nm at the focus of a 35 cm telescope.

7.5 cm, 12 cm, 15 cm, 18 cm, 22 cm, and 30 cm at the observation wavelength (700 nm), corresponding to D/r_0 ratios from ∼3.5 to ∼14. The vertical repartition of the turbulence for these simulations is detailed in Table 1, together with the other relevant physical and numerical parameters.

In order to compare the PSE method with other LI techniques, we did simulations which can be targeted as optimistic, in the sense that neither a possible readout noise nor a realistic temporal evolution of the images are taken into account. In fact, we have considered that in the case of EMCCD cameras in which we are particularly interested, readout noise becomes negligible. Also, images are considered as instantaneous with respect to temporal evolution of turbulence, and images are statistically independent (no temporal evolution of the deformed wavefronts and hence the subsequent images is considered). We also did consider the monochromatic case only: there is no modeling of the smearing effect due to the actual width of the spectral filter in use (a bandwidth was nonetheless considered for the conversion from photon numbers to magnitudes in the examples given hereafter). In the other hand, we did have considered the lack of low spatial frequency suffered by the FFT-based numerical methods permitting the simulation of atmospherically perturbed phase screens Lane et al. (1992), Sedmak (1998), and the right number of subharmonics Carbillet et al. (2011) have been added in order to overcome this well-known problem.

To check the performances of the method in case of low-light levels, photon noise was also introduced on the short-exposure frames. We have so tested different numbers of photons per image N: 100, 1000, 10,000, and 100,000. We eventually chose $N = 100$ photons/image as our low photon level case, and, since we found no significant difference between $N = 10{,}000$ photons/image and $N = 100{,}000$ photons/image, we chose $N = 10{,}000$ as our high photon level case. In the case of a 1 m telescope in R band with a bandpass $\Delta\lambda = 100$ nm, an exposure time of 10 ms, and an overall efficiency (including instrumental transmission) of 30%, the case $N = 10{,}000$ (respectively $N = 100$) corresponds to a magnitude of 8.7 (respectively 13.7).

Table 1
C_N^2 Profile Model Adapted from Voyez et al. (2014) and Other Parameters Considered for the Simulations

turbulent atmosphere	
Fried parameter r_0 (at 500 nm)	5–20 cm
turbulent layers' altitudes	[0, 0.5, 3, 6, 10, 13, 16.5] km
turbulent layers' relative C_N^2	[69, 10, 4, 6, 9, 4, 2, 2] %
wave front outer-scale $\mathcal{L}_0$	27 m
observing telescope	
diameter D	1.04 m
number of pupil pixels	128 × 128
⇒ wave front pixel size	0.8125 cm
obscuration ratio	0.26
image formation	
imaging wavelength λ	700 nm
number of image pixels	128 × 128
image pixel size Δx	$0\farcs035$ ($\simeq\frac{\lambda}{4D}$)
⇒ field of view	$4\farcs48$
number of photons per image N	[100, 10,000]

Figure 1 (left) shows an example of a short-exposure PSF without photon noise. Images of observed objects (double stars and a simulated artificial satellite) were obtained by convolution of the extended object with each short-exposure image, photon noise being introduced after the convolution. Figure 2 shows an example of an image of an artificial satellite of angular size $10\,\lambda/D$ ($\sim 1\farcs4$) with $r_0 = 20$ cm at the two selected light levels: $N = 10{,}000$ photons/image (middle) and N = 100 photons/image (right).

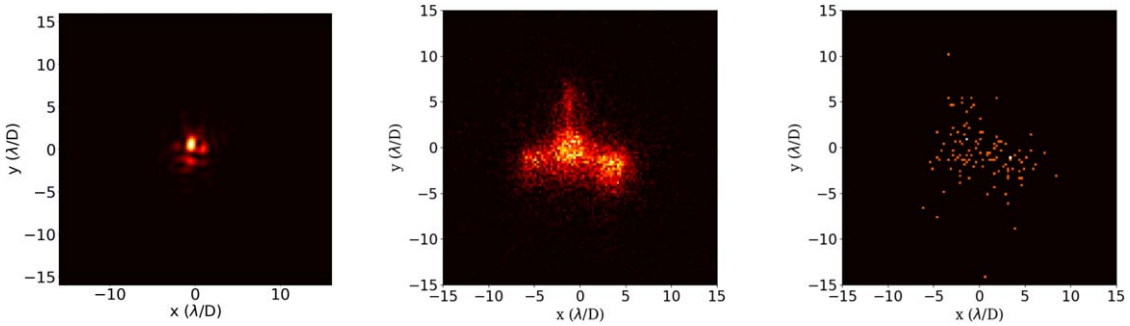

Figure 2. Simulation of a short-exposure with $r_0 = 20$ cm. Left: PSF without photon noise. Middle: corresponding image of a satellite with 10,000 photons/image. Right: same object and same PSF but with 100 photons/image.

2.3. Selection and Classification

Image selection is a very important part of LI algorithms. It is often made by estimating a Strehl ratio on a bright star in the field Garrel et al. (2012), but this method is not suitable for extended objects. We propose here an image selection based on the estimation of an "instantaneous Fried parameter", an idea already used in speckle data processing Aristidi et al. (1997).

Indeed, for Kolmogorov turbulence, the speckle transfer function $W(u, v)$ exhibits a low frequency part which can be expressed, for low angular frequencies ($||\boldsymbol{u}|| < \frac{r_0}{\lambda}$), as Fried (1966), Roddier (1981):

$$W(u, v) = \exp\left\{-6.88\left(\frac{\lambda||\boldsymbol{u}||}{r_0}\right)^{\frac{5}{3}}\right\}. \quad (1)$$

Inverting this relation makes it possible to obtain an estimate of the Fried parameter:

$$r_0 = \lambda||\boldsymbol{u}||\left(-\frac{6.88}{\ln\{W(u, v)\}}\right)^{\frac{3}{5}}, \quad (2)$$

with $||\boldsymbol{u}|| = \sqrt{u^2 + v^2}$ the modulus of the spatial frequency vector.

Within our data processing, we hence compute an estimate of $W(u, v)$ as the power spectrum of individual frames, and obtain an instantaneous Fried parameter. Several estimations of r_0 are calculated on both directions u and v and averaged.

This classification was tested on simulations described in Section 2.2. A data cube of 6000 images of a point-source with various turbulence conditions was generated and classified using our criterion based on the instantaneous Fried parameter. Results are shown in Figure 3. It is a plot of the estimated value of r_0 as a function of the actual value of the Fried parameter used in the simulations. Both parameters show a good correlation, and there is a clear linear relation in between them. However, they are not equal: our method provides only a relative estimator of r_0, but this is sufficient for image classification. To study the pertinence of our classification, we calculated the Strehl ratio of reconstructed PSFs corresponding

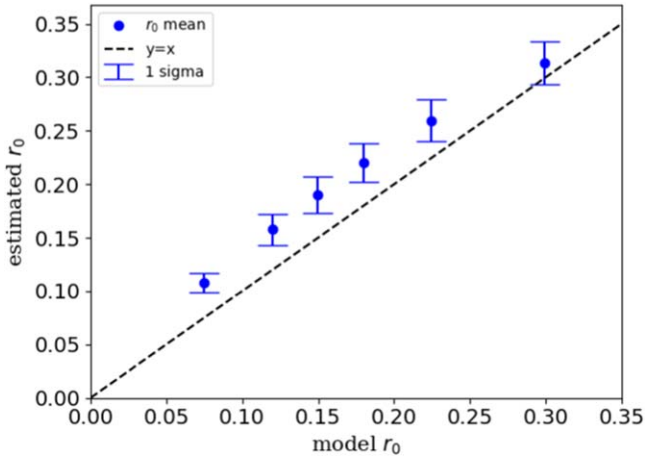

Figure 3. Instantaneous Fried parameter estimated on simulated short-exposure PSF images (Equation (2)) against theoretical r_0 values used for the simulation.

to different values of the estimated r_0. The results are displayed in Figure 4 (left). One can see that large r_0 values correspond to large Strehl ratios, as expected. In order to compare our selection method with the classical selection by means of the Strehl ratio, we applied both methods to the same data on PSF images. The result is shown in Figure 4 (right), which displays the Strehl ratio of the reconstructed image as a function of the selection rate. We found that the two selection processes are equivalent for objects where a point-like source dominates, with a slight advantage for the Strehl selection in the case of low selection rate.

The method applies also to extended objects. In this case, the power spectrum in Equation (1) is multiplied by a function of $\boldsymbol{u}$. This function is the object square visibility and is the same whatever the turbulence conditions. In that case the r_0 deduced from Equation (2) is no more a Fried parameter, but has small (respectively high) values for poor (respectively good) turbulence conditions. Therefore, it provides also a relative estimator to classify images.

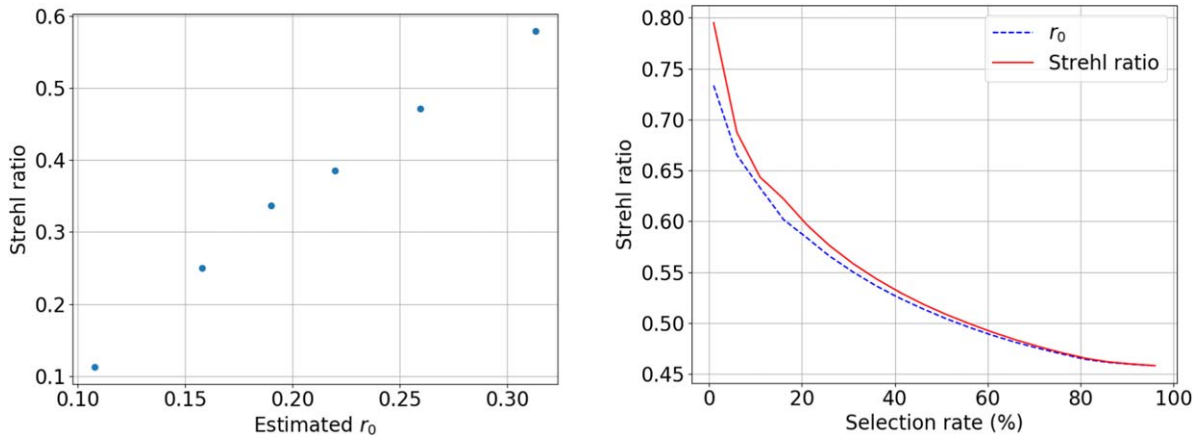

Figure 4. Left: Strehl ratio of reconstructed PSFs as a function of the estimated Fried parameter. Right: Strehl ratio of reconstructed PSFs as a function of the selection rate, with both a classical Strehl selection and our proposed r_0-based selection method.

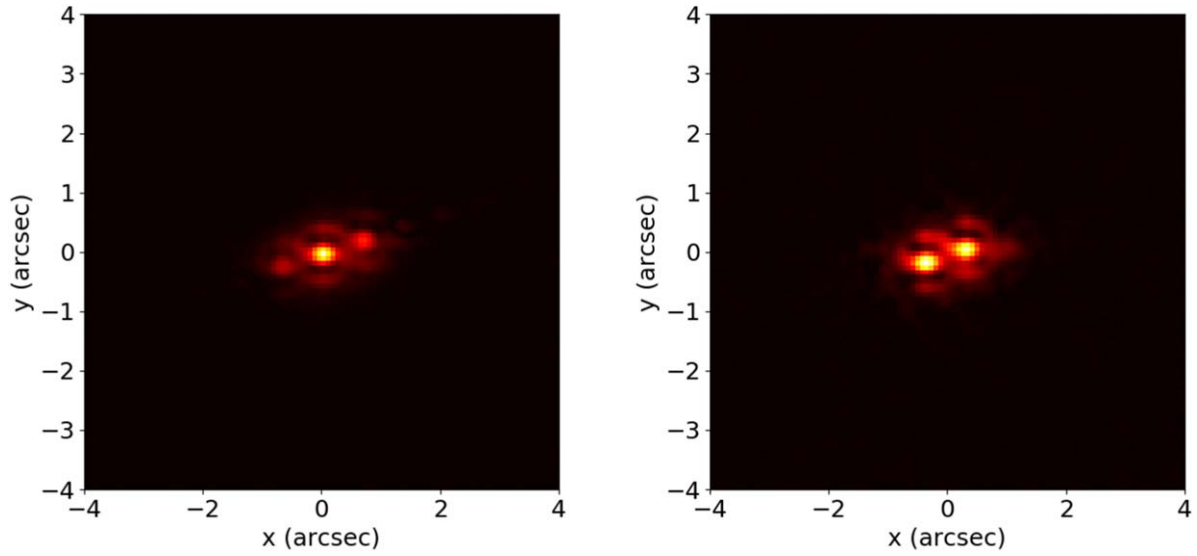

Figure 5. Reconstructed images of the binary star *i Boo*, based on short exposures obtained with one of the 1.04 m telescopes of C2PU. Left: LI reconstruction using a classical SaA method based on the centroid. Right: same but with our alignment method.

2.4. Alignment of Short-exposure Frames

In LI techniques, the alignment of the short-exposure frames is generally based on the centroid calculated around the brightest pixel of the image Baldwin et al. (2001). A correct alignment is indeed critical for image reconstruction, and the centroid method does not give good results in some cases, for example in the case of a double star with a similar magnitude for both components, but also for homogeneous extended sources.

As an illustration of this problem, we applied both LI and PSE on short-exposure images of the binary star *i Boo*, observed with the telescope Epsilon of C2PU in the near-infrared (H band, see Aristidi et al. 2020 for more details on these observations), a binary star with a small magnitude difference ($\Delta m = 0.09$). Figure 5 (left) shows the reconstructed image using an LI algorithm based on the centroid computation. We notice the presence of a ghost image of the companion, evidently due to a bad alignment. In order to avoid such an artifact, we propose here a method to align images which works in the Fourier domain.

The underlying idea is to take advantage of a property of the FT. In fact, shifting an image by a quantity $\Delta\boldsymbol{r}$ is equivalent to multiply by a phase term within the Fourier space:

$$\mathcal{F}[I(\boldsymbol{r} + \Delta\boldsymbol{r})] = \mathcal{F}[I(\boldsymbol{r})] \cdot e^{2i\pi\boldsymbol{u}\cdot\Delta\boldsymbol{r}}, \quad (3)$$

with $\mathcal{F}[\star]$ the FT of $\star$, $I(\boldsymbol{r})$ the image intensity distribution, $\boldsymbol{r} = (x, y)$ the spatial position vector, $\boldsymbol{u} = (u, v)$, the spatial

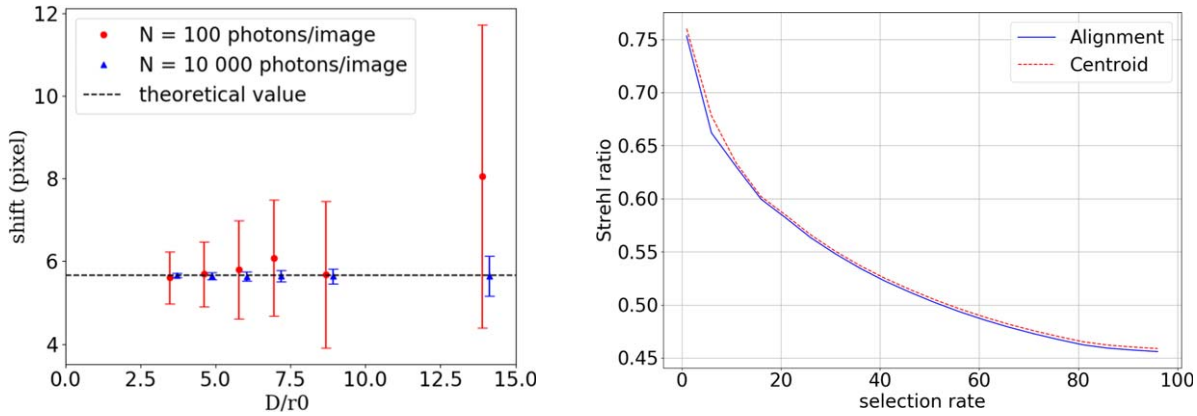

Figure 6. Left: measured shift as a function of the ratio D/r_0 characterizing the data, and for two values of the number of photons/image: $N = 100$ (circles) and $N = 10{,}000$ (triangles). To improve the visibility, we applied a small horizontal shift to the points corresponding to $N = 10{,}000$ (triangles). The error bars show the resulting rms from 50 independent photon noise realizations. Right: Strehl ratio against the selection rate for both the conventional centroiding alignment and our proposed alignment method.

frequency vector, $\Delta\boldsymbol{r}$ the spatial shift vector. From Equation (3), one can then write the phase of the cross-spectrum Φ as the phase difference between the FT of the shifted image and the FT of the non-shifted image:

$$\Phi(\boldsymbol{u}) = \varphi_{\boldsymbol{r}+\Delta\boldsymbol{r}}(\boldsymbol{u}) - \varphi_{\boldsymbol{r}}(\boldsymbol{u}) = 2\pi\boldsymbol{u} \cdot \Delta\boldsymbol{r}, \tag{4}$$

where $\varphi_{\boldsymbol{r}}(\boldsymbol{u})$ is the phase of the FT of $I(\boldsymbol{r})$.

To align two successive images, we hence compute the phase of their cross-spectrum and perform a linear fit on the spatial frequency directions u and v in order to estimate their relative shift $\Delta\boldsymbol{r}$. The second image is then aligned to the first one by multiplying its FT by the correcting term $e^{-2i\pi\boldsymbol{u}\cdot\Delta\boldsymbol{r}}$. To align all frames of the image cube, we also chose to perform a gliding alignment: the second image is aligned with the first, the third image is aligned with the second, and so on.

The alignment process was tested on simulated PSF cubes from different values of r_0, with our two photon noise levels, and for 50 independent realizations. Each PSF was shifted by 4 pixels in both directions x and y. The shift was then estimated from the slope of the phase of the cross-spectrum and an ensemble average was computed on the set of 1000 images and of 50 realizations of the photon noise. Figure 6 (left) shows the estimated shift as a function of the ratio D/r_0 for the two values of N. In the case of high-light level, the estimation is accurate ($\sim$0.05 pixel) for all the D/r_0 ratios, while for the case of low-light level, the error is clearly superior and spectacularly grows with the largest value of D/r_0. If one compares this alignment method with a classical centroiding algorithm (see Figure 6, right), it appears that the two methods show equivalent performance in terms of Strehl ratio.

This alignment process also performs very well on extended objects. Figure 7 shows an application to real data. The processed image cube consists of 1000 snapshots of the planet Mars, taken with a 0.35 m diameter telescope at $\lambda = 700$ nm. The left image is reconstructed via a classical LI process based on the centroid, with a selection of 20% of the images. As it can be seen, the center of individual images is not estimated correctly, resulting into a completely blurred reconstructed image. On the contrary, the right-hand side image shows the convincing result of using our cross-spectrum-based alignment process.

2.5. Recovery of the Modulus of the FT

In order to recover the modulus of the FT of the image of the observed object, we use the Labeyrie's SI technique Labeyrie (1970). We compute the average power spectrum of selected short-exposure images and take its square root to obtain the modulus of the FT.

The power spectrum for an image limited by the photon noise is the sum of two terms, the power spectrum of the object and a constant bias term Goodman (1985), Aime & Aristidi (1992). In order to subtract the bias, we compute the median of power spectrum values beyond the cut-off frequency.

A comparison is provided by Figure 8. We used simulated PSF cubes (see Section 2.2) for different ratios D/r_0, and reconstructed the diffraction-limited image (here an Airy disk) by a classical SaA algorithm with no image selection. We compare the modulus of the FT of the resulting image with the square root of the power spectrum, for the two light level regimes. The gain is noticeable in the high frequency part, indeed for 10,000 photons/image and $D/r_0 = 8.7$, we have a ratio of $\sim$5 between the two quantities.

2.6. Recovery of the Phase of the FT

In the PSE processing, the phase of the FT of the object is obtained from the image reconstructed by a shift-and-add process applied to selected (see Section 2.3) and aligned (see Section 2.4) short-exposure frames. One of the main ideas

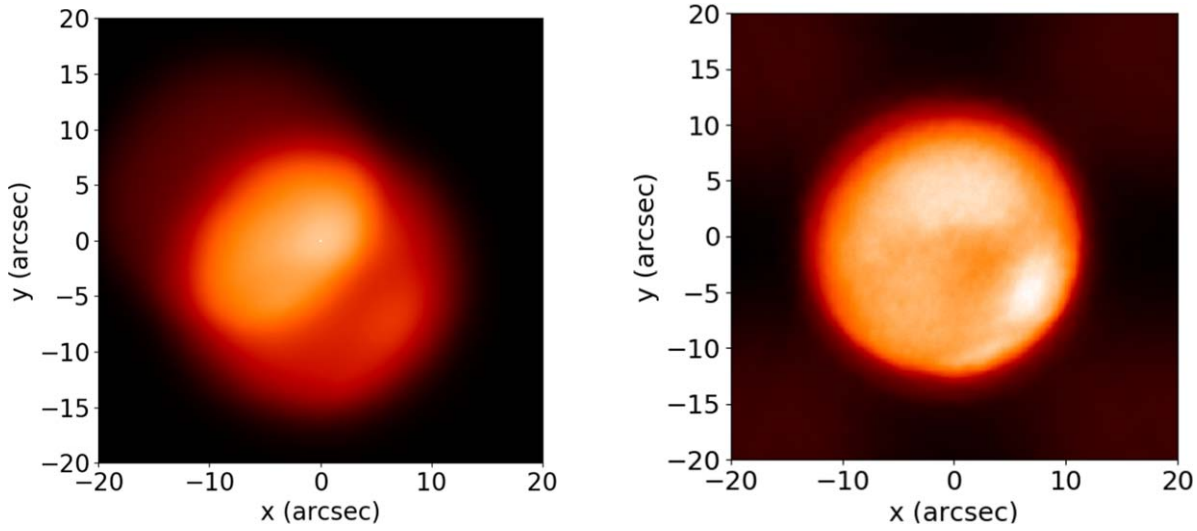

Figure 7. Reconstructed images of Mars, based on 1000 short-exposure images at the focus of a 0.35 m telescope, at $\lambda = 700$ nm. Left: LI reconstruction using an alignment based on the centroid, with an image selection rate of of 20%. Right: PSE reconstruction (alignment based on the slope of the phase of the cross-spectrum), with the same image selection rate.

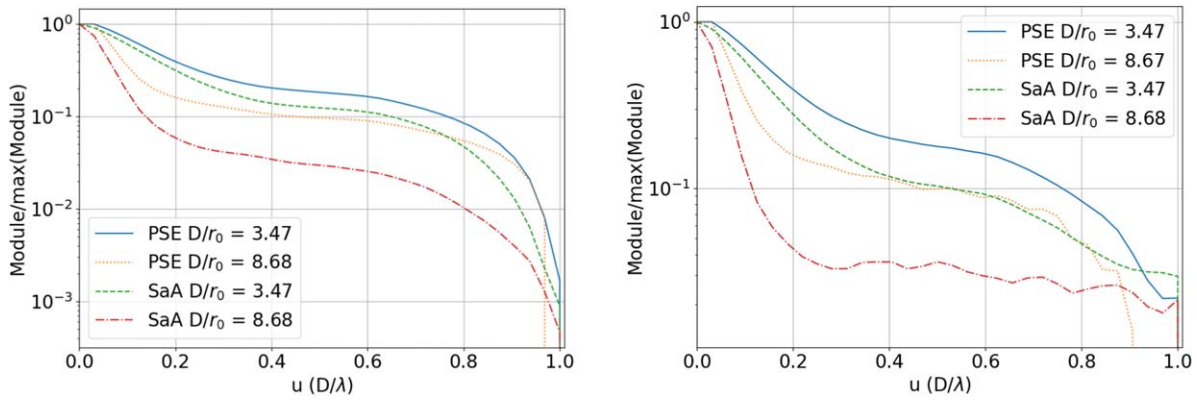

Figure 8. Modulus of the FT of the image reconstructed by a shift-and-add process from a simulated PSF cube of 1000 short-exposure frames, compared to the square root of the power spectrum used for PSE. Left: 10,000 photons per image. Right: 100 photons per image.

behind LI is that for low turbulence conditions (e.g., low D/r_0 ratio), the dominant effect is the tip-tilt. Hence short-exposure frames still contain information about the shape of the observed object. By correcting the tip-tilt (i.e., by applying an SaA algorithm to short-exposure frames), it is possible to recover an image of the object. In the PSE processing, the phase of the FT of this SaA image is taken as the estimate of the phase of the FT of the object.

We performed a numerical simulation to illustrate the performances of this phase estimation. We generated a cube of 1000 short-exposure images of a binary star with an intensity ratio of 5 and an angular separation of $4\lambda/D$ for two turbulence conditions ($D/r_0 = 3.47$ and $D/r_0 = 8.68$) and our two light levels. We calculated the phase of the shift-and-add (PSE with no image selection) image in all four cases, and compared it with the phase of the long-exposure image (without tip-tilt compensation). Results are shown in Figure 9. For the high-light level case (left), the phase shows a sinusoidal curve which agrees perfectly with the theoretical phase (black crosses) up to the telescope cut-off frequency for both D/r_0 ratios. The phase of the long-exposure image (labeled LP within the figure) does also show a sinusoidal behavior, but only in the low frequency part of the graph. For the low-light level (right), the phase still agrees with the theoretical sinusoid but the agreement is better when the turbulence is low ($D/r_0 = 3.47$).

3. Comparison with ISFAS

ISFAS is a LI technique Garrel et al. (2012) which can be considered one of the most efficient. It has common points with

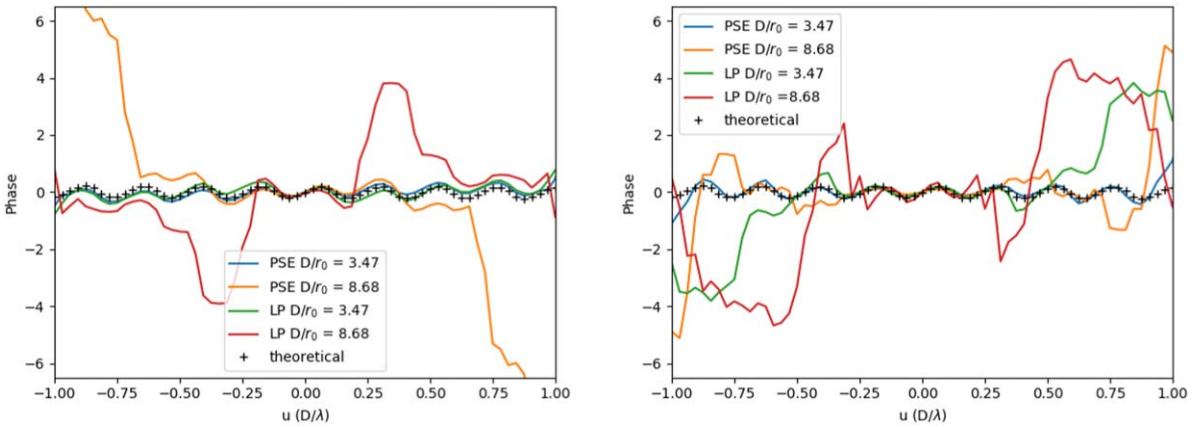

Figure 9. Phase of the FT of the image reconstructed from a simulated cube of 1000 short-exposure images of a binary star with an intensity ratio of 5 and a separation of $4\lambda/D$. Left: high-light level (10,000 photons/image), right: low-light level (100 photons/image). Curves labeled as PSE denote a reconstruction by the PSE algorithm. Curves labeled as LP denote the long-exposure image, and black crosses the theoretical phase.

PSE as it operates in the Fourier plane. In the ISFAS method, the selection is performed on the modulus of the FT, frequency by frequency. For selected images, an average of complex Fourier transforms of images is calculated for each frequency. Before the selection, each modulus is convolved with a small spatial Gaussian kernel to average the photon noise. The reconstructed image is then obtained by taking an inverse Fourier transform. In this section, we make a comparison between images reconstructed by PSE and images reconstructed by ISFAS, for different kinds of simulated objects (PSF, binary stars, artificial satellite). We also compare performances of both algorithms for different numbers of photons and selection rates.

3.1. Results on Simulated PSF

Our first comparison is based on simulated PSF cubes (Section 2.2). For this comparison we use the Strehl ratio as the metrics for the quality of reconstructed images, since the Strehl ratio is a classical metrics to estimate the quality of reconstruction in LI techniques (see for example Baldwin et al. 2001; Basden et al. 2004).

The Strehl ratio S can be estimated by means of Equation (5) of Tokovinin (2002):

$$S = \frac{I_{\max}}{I_{\text{tot}}} \frac{4}{\pi} \left(\frac{\lambda}{D\Delta x} \right)^2, \tag{5}$$

with I_{tot} and $I_{\max}$ respectively the total and maximum intensity, and Δx the pixel size in radians.

Figure 10 shows an example of reconstructed PSF obtained from a data cube as presented in Section 2.2 The selection rate was 10% and the number of photons per image was $N = 100$. Both images are near the diffraction-limit and show the first bright Airy ring, but the Strehl ratio is higher for PSE (Strehl ratio of 0.55 for PSE against 0.2 for ISFAS).

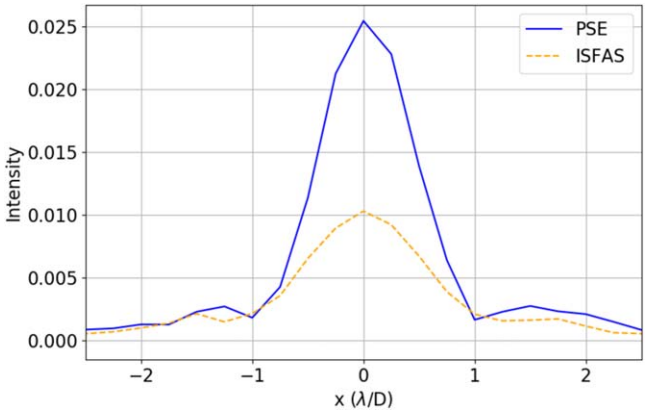

Figure 10. Cut of the reconstructed PSF from a simulated image cube containing 6000 short-exposure frames with different turbulence conditions ($r_0 \in$ [5–20]cm), with a selection rate of 10% and 100 photons per image. Blue curve: PSE (Strehl ratio of 0.55), red curve: ISFAS(Strehl ratio of 0.20).

Figure 11 shows the Strehl ratio of reconstructed PSF as a function of the selection rate for $N = 100$ and $N = 10{,}000$ photons per image. We can notice that the Strehl ratio for PSE is higher than ISFAS, both for low- and high-light levels. Indeed for a selection rate of 10% in the case of low-light level, we obtained a Strehl ratio of 0.55 for PSE against 0.2 for ISFAS—with $N = 10{,}000$, the Strehl ratios were respectively 0.59 and 0.41. We can also notice that the Strehl ratio obtained by both techniques decreases as the selection rate increases. However this drop is more pronounced for ISFAS (especially at high-light level), which appears to be more sensitive to image selection.

3.2. Results on a Simulated Double Stars

Our second comparison is based on the relative photometry of binary stars, which are a prevailing science case for passive

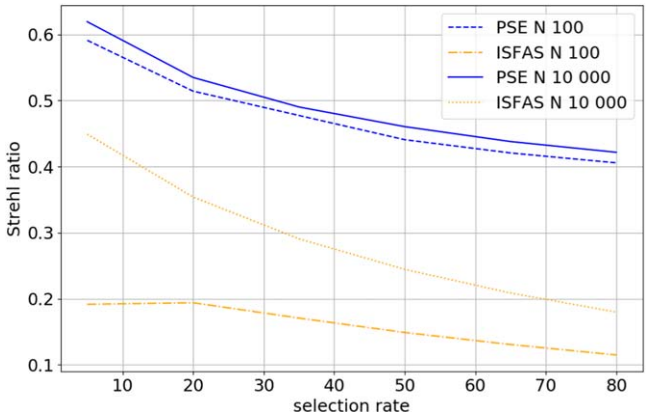

Figure 11. Strehl ratio for reconstructed PSF for PSE and ISFAS as a function of the selection rate, at high-light level (10,000 photons per image) and low-light level (100 photons/image).

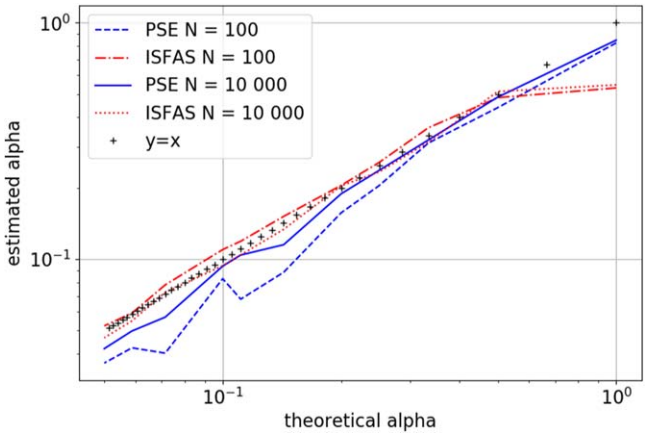

Figure 12. Intensity ratio α_{esti} estimated on reconstructed images as a function of the modeled value α_{theo}, for the two reconstruction algorithms PSE and ISFAS, and for two number of photons per images ($N = 100$ and $N = 10,000$). The selection rate is 20%.

HAR techniques. A widely accepted metric of performance for this case is the precision of determination of binary star parameters Lillo-Box et al. (2014), Tokovinin (2010). In a previous communication Aristidi et al. (2020), we applied the PSE algorithm to double stars observed in the infrared with a 1 m telescope, and compared the precision on astrometric parameters (angular separation and position angle) with other techniques (ISFAS, SaA and SI). In this paper, we focus on the determination of the relative photometry, i.e., the intensity ratio between the two stars. Our study is based on simulated cubes of double stars, with a separation $\rho = 10\lambda/D$ and an intensity ratio α between 0.05 and 1. The ideal binary object is modeled by the sum of two impulse functions $\delta(\boldsymbol{x}) + \alpha \cdot \delta(\boldsymbol{x} - \rho)$ with $\boldsymbol{x}$ the angular position vector in the image. We applied the two algorithms (PSE and ISFAS) to simulated cubes under two photon noise levels, 100 and 10,000 photons per image, and a selection rate of 20%. The estimation of the intensity ratio α was made by using a classical aperture photometry technique Howell (1989) on each star on reconstructed images.

The results are presented in Figure 12. We show the estimated intensity ratio α_{esti} as a function of the theoretical ratio α_{theo}, for ISFAS and PSE and for the two number of photons/image. Both methods perform well at high light level, excepted for ISFAS in the case $\alpha = 1$. This is a consequence of the "ghost" effect described in Section 2.4. At low light level, however, PSE shows more instability and tends to underestimate the intensity ratio for small values of α.

3.3. Results on a Simulated Satellite

In this section we present an application of the PSE technique to a simulated satellite. The object is an artificial satellite with an angular size of $\sim 10\,\lambda/D$. This size was chosen so that the satellite remains smaller than the isoplanatic angle, typically a few arcsec at this wavelength. The diffraction-limited image of this satellite is shown in Figure 13 (left). Both PSE and ISFAS algorithms were applied to simulated short-exposure frames of the satellite under different photon noise levels. Reconstructed images are shown in Figure 13 for $N = 10{,}000$ photons per image. The PSE output appears to be more faithful to the diffraction-limited image, in particular the halo is smaller than for the ISFAS image, and high resolution details such as satellite edges appear more clearly.

To quantify the quality of the reconstruction, we used a metrics based on a relative least-square distance d between the reconstructed image and the satellite diffraction-limited image:

$$d = \frac{\int (I(\boldsymbol{r}) - I_{DL}(\boldsymbol{r}))^2 \, d\boldsymbol{r}}{\int I_{DL}(\boldsymbol{r})^2 \, d\boldsymbol{r}},$$

where $I(\boldsymbol{r})$ (resp. $I_{DL}(\boldsymbol{r})$) is the reconstructed image (resp. the diffraction-limited image) normalized so that its integral is equal to 1, and $\boldsymbol{r} = (x, y)$ the angular position vector.

Figure 14 shows the distance d as a function of the selection rate for the two methods, both for $N = 100$ and $N = 10{,}000$ photons per image. We can notice that the distance is lower for PSE than for ISFAS in all cases. Hence the PSE image appears closer to the diffraction-limited image than the ISFAS one. For example, at low-light level, and with a selection rate of 10%, we get a distance $d = 0.6$ for PSE against $d = 0.7$ for ISFAS.

3.4. Computational Speed

Computation time is a challenge for real-time image reconstruction. In particular, LI algorithms need a first analysis of the whole data set for image selection before doing the actual reconstruction. The whole process can be somewhat slow. It

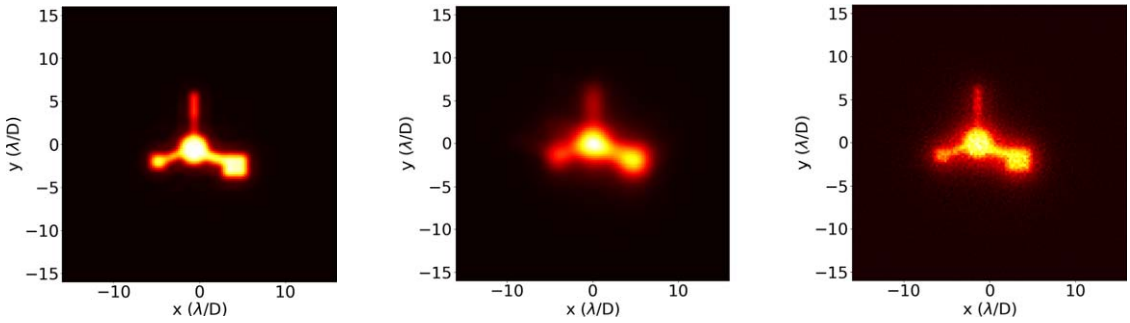

Figure 13. Reconstructed image of a simulated artificial satellite from 6000 short-exposure frames with different r_0 (5–20cm) and 10,000 photons per image. The selection rate was 20%. Left: diffraction-limited image of the satellite. Middle: ISFAS reconstruction. Right: PSE reconstruction.

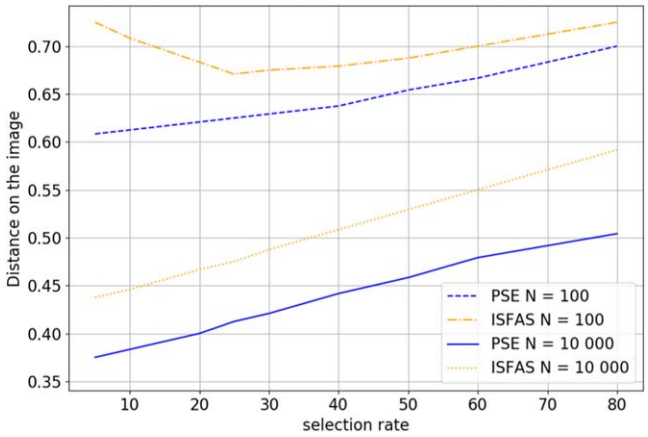

Figure 14. Distance d for the PSE and the ISFAS techniques, both for $N = 100$ and $N = 10{,}000$ photons per image.

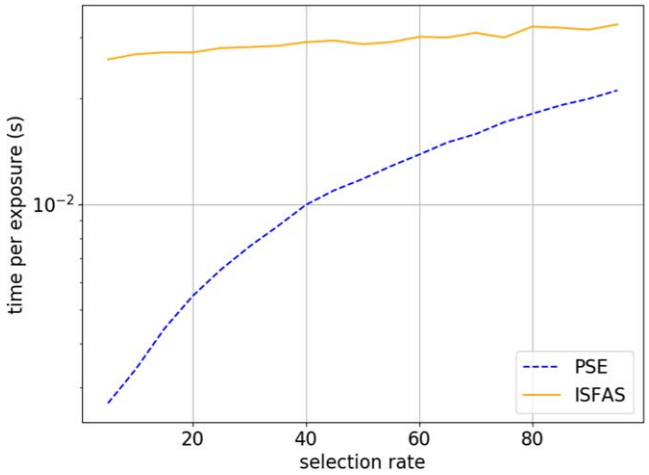

Figure 15. CPU time per image for the reconstruction of a PSF using PSE and ISFAS algorithms, as a function of the selection rate (see text for details).

appears that PSE has the advantage to be very fast, compared to ISFAS.

In this section, we compare computational speed for the two methods, estimating the time of reconstruction of the object from a simulated data cube of 6000 short-exposure images with various turbulence conditions, as described in Section 2.2. We made these simulations at low-light level ($N = 100$ photons per image).

This benchmark was realised on a PC equipped with an Intel® Core™ i7-8850H processor, with a frequency of 2.60 GHz and 32 GB memory. The programming language was Python. The computation time was determined for different selection rates.

Results are presented in Figure 15. We have plotted the time of execution per image against the selection rate. We can notice that PSE is faster than ISFAS for low selection rates. As an example, for a selection rate of 10%, we get 3.4 ms per image for PSE against 25.3 ms for ISFAS. This is a gain of CPU time of a factor ∼7, which opens interesting perspectives for near real-time PSE processing.

4. Summary and Discussion

In this paper, we have analyzed the LI technique PSE for reconstruction of images distorted by atmospheric turbulence. It mixes a shift-and-add algorithm with speckle techniques. We also propose new ideas to select and align short-exposure frames. The application of these techniques to real speckle data, shown in Section 2.1, looks encouraging. This technique can also be applied to post-AO short exposure images, and first attempts were presented in Cottalorda et al. (2020).

The performance of the technique was investigated by means of numerical simulations, with different turbulence regimes, at high- and low-light levels, and for different kinds of objects. The PSE technique looks promising, and provides satisfactory image reconstruction for low D/r_0 ratios. PSE improves three main steps of the LI processing: the image alignment, the image selection, and use of the average power spectrum on instantaneous images to replace the modulus of the long-exposure image. It provides images with more details than classical LI algorithms as high angular frequencies are

enhanced. It also solves centering problems with extended sources or double stars with low magnitude difference. Its performances appear to be similar or superior to the ISFAS method for extended objects or images of PSFs. But ISFAS seems to perform better for relative photometry of double stars having a large intensity ratio.

One of the main advantages of PSE is the speed of reconstruction: a few milliseconds are required to process an image, this opens the possibility to perform near real-time image reconstruction, which is particularly interesting for rapidly changing objects such as moving artificial satellites. Another advantage is its simplicity: it is very easy to implement and this could be interesting for educational purposes too.

A drawback of PSE is the lack of compensation of the STF in the power spectrum of images, as it is done in speckle processing, but this is a criticism that can be made to other LI or SaA algorithms. There is room for improvement here, and we plan to work on this point in the future.

The authors wish to thank deeply the anonymous referee for his thorough reading of the manuscript. This work is part of the PhD thesis work of Éric Cottalorda, done within the framework of a CIFRE convention between Ariane Group and the Centre National de la Recherche Scientifique (CNRS) through its Lagrange laboratory (Université Côte d'Azur, Observatoire de la Côte d'Azur, CNRS).

References

Aime, C., & Aristidi, E. 1992, JOSAA, 9, 1812
Aristidi, E., Carbillet, M., Prieur, J. L., et al. 1997, A&AS, 126, 555
Aristidi, E., Cottalorda, E., Carbillet, M., et al. 2020, Proc. SPIE, 11448, 114484Z
Baba, N., Isobe, S., Norimoto, Y., & Noguchi, M. 1985, ApOpt, 24, 1403
Baldwin, J. E., Tubbs, R. N., & Cox, G. C. 2001, A&A, 814, 803
Basden, A., Mackay, C., Haniff, C., et al. 2004, "Scientific Detectors for Astronomy, The Beginning of a New Era" (Berlin: Springer), 599
Bendjoya, P., Abe, L., Rivet, J.-P., et al. 2012, in SF2A 2012: Proc. Ann. French Soc. Astron. Astrophys., ed. S. Bossier, P. de Laverny, & N. Nardetto (Paris: SF2A), 643
Carbillet, M., Vérinaud, C., Femenìa, B., Riccardi, A., & Fini, L. 2005, MNRAS, 356, 1263
Carbillet, M., Vérinaud, C., Femenìa, B., Riccardi, A., & Fini, L. 2011, CAOS: Code for Adaptive Optics Systems, ascl:1106.017
Carbillet, M., La Camera, A., Folcher, J.-P., & Perruchon-Monge, U. 2016, Proc. SPIE, 9909, 99097J
Cottalorda, E., Aristidi, E., Carbillet, M., Guinard, M., & Vourc'h, S. 2019, in SF2A 2019: Proc. Ann. French Soc. Astron. Astrophys., ed. P. Di Matteo, O. Creevey, & A. Crida (Paris: SF2A), 215
Cottalorda, E., Aristidi, E., Carbillet, M., Guinard, M., & Vourc'h, S. 2020, Proc. SPIE, 11448, 1144850
Femenía, B., Rebolo, R., Pérez-Prieto, J. A., et al. 2011, MNRAS, 413, 1524
Fried, D. L. 1966, JOSA, 56, 1372
Fried, D. L. 1978, JOSA, 68, 1651
Garrel, V., Guyon, O., Baudoz, P., et al. 2012, PASP, 124, 861
Goodman, J. 1985, Statistical Optics (New York: Wiley)
Howell, S. B. 1989, PASP, 101, 616
Knox, K. T., & Thompson, B. J. 1974, ApJL, 193, L45
Labeyrie, A. 1970, A&A, 6, 85
Lane, R. G., Glindeman, A., & Dainty, J. C. 1992, Waves Random Media, 2, 209
Lillo-Box, J., Barrado, D., Henning, T., et al. 2014, A&A, 566, A103
Mackay, C., Rebolo-López, R., Femenia, C., et al. 2012, Proc. SPIE, 8446, 844621
Roddier, F. 1981, Progress in Optics, Vol. 19 (Amsterdam: North-Holland Publishing Co.), 281
Scardia, M., Rivet, J.-P., Prieur, J.-L., et al. 2019, AN 340, 771
Sedmak, G. 1998, ApOpt, 37, 4605
Tokovinin, A. 2002, PASP, 114, 1156
Tokovinin, A. 2010, AJ, 139, 743
Voyez, J., Robert, C., Conan, J.-M., et al. 2014, Opt. Express, 22, 10948
Weigelt, G. 1991, Progress in Optics, XXIX (Amsterdam: Elsevier), 293
Worden, S. P., Stein, M. K., Schmidt, G. D., & Angel, J. R. P. 1977, Icarus, 32, 450